

Research Article

Axial Cyclic Testing of Concrete-Filled Steel Tube Columns in Diagrid Structures

Qingxuan Shi,^{1,2} Wenzhe Cai ,¹ and Bin Wang ^{1,2}

¹State Key Laboratory of Green Building in Western China, Xi'an University of Architecture & Technology, Xi'an 710055, China

²School of Civil Engineering, Xi'an University of Architecture & Technology, Xi'an 710055, China

Correspondence should be addressed to Bin Wang; wangbin@xauat.edu.cn

Received 20 November 2018; Accepted 2 April 2019; Published 2 May 2019

Academic Editor: Humberto Varum

Copyright © 2019 Qingxuan Shi et al. This is an open access article distributed under the Creative Commons Attribution License, which permits unrestricted use, distribution, and reproduction in any medium, provided the original work is properly cited.

Inclined concrete-filled steel tube (CFST) columns in a diagrid structure system can efficiently carry large vertical loads and horizontal forces. This paper presents an experimental study of the stress characteristics of engineered inclined CFST columns under axial cyclic loading. Ten specimens were tested, including two hollow steel tube (HST) columns and eight CFST columns, and the influences of loading scheme, aspect ratio, concrete strength, and steel ratio were examined. The seismic behaviours were investigated, including mechanical behaviour, failure modes and hysteretic curves, and ductility, and the interaction between the steel tube and concrete was examined as well. Better ductility and energy dissipation capacity are achieved in the tension direction, whereas higher bearing capacity and stiffness are achieved in the compression direction. Compared with hollow steel tube columns, the supporting effect of concrete on the steel tube for CFST columns in tension and the restraining effect of the steel tube on concrete for CFST columns in compression ensure higher capacity, deformability, and energy dissipation capacity.

1. Introduction

With increasing building height, structural lateral displacement has become the main control target in design, and therefore, high-rise buildings should not only supply sufficient bearing capacity but also offer sufficient lateral rigidity. Diagrid structural systems have become an increasingly attractive choice for mid- to high-rise buildings worldwide. The main distinction between the diagrid structure and conventional structural systems is the absence of vertical members in the structure, which are replaced with inclined brace-shaped members known as diagonals. This arrangement is possible because the diagonal members can carry gravity loads as well as lateral forces due to their triangulated configuration and can also convert the load into axial tension and compression for downward transfer. In contrast, the diagonals in conventional braced-frame structures only undertake lateral loads. Because the axial stiffness of the diagonal is far greater than the lateral stiffness, the diagrid structure formed by the inclined column has greater resistance to lateral stiffness,

and the transmission force of the inclined column is more direct and has a stronger spatial coordination performance. Stated thus, diagrid structural systems have potential advantages in construction of super-high-rise buildings and have been increasingly used in modern architecture, e.g., the Swiss Re Building in the United Kingdom, the Hearst Headquarters in the United States, the Ministry of Foreign Affairs in Qatar, the Lotte Super Tower in Korea, and the Western Tower in Guangzhou, China. However, theoretical research on the diagrid structure lies far behind engineering practice. No unified design methodology has yet been formulated, and little research has focused on the diagonals.

A few research papers have examined diagrid performance assessment under extreme events. Lee et al. [1] presented a comparative study on the seismic performance evaluation of circular- and square-shaped diagrids based on the diagonal angle effect on the nonlinear behaviour of diagrid systems. Zhou and Wang [2] noted that the inclined columns were primarily subjected to axial load in elastic-plastic analysis of structural under vertical and horizontal

loads. Specifically, Zhao [3] and Guo [4] reported that the inclined columns at the bottom of the structure all bear the axial pressure, whereas the inclined column experiences tension force in the upper floor of the high intensity zone, according to the seismic performance analysis of the diagrid structure, and thus the CFST column is subjected to axial cyclic tension and compression loads under earthquakes. For the components, Zhou et al. [5], Kim et al. [6], and Han et al. [7] conducted pseudostatic tests on intersecting nodes in the diagrid structure and analysed the force mechanism and hysteresis performance under axial cyclic loads; however, the relevant research on inclined CFST columns in diagrid structures is still in the initial stage. Currently, the studies on CFST columns mainly focus on the monotonic behaviour of vertical bearing members and the seismic performance of lateral force-resistance components [8–15], while minimal research has focused the mechanical behaviour under cyclic loads of components such as lateral braces [16, 17], and few studies have been conducted on the mechanical behaviour of the inclined CFST columns under cyclic axial loads, which are the major components of the diagrid structure. Therefore, the study of the bearing mechanism and seismic performance of the CFST columns under axial cyclic loads is an urgent need.

Based on the current status, eight CFST columns and two hollow steel columns were designed for application in seismic performance tests aimed at studying the stress mechanism and failure modes under axial cyclic loads. The effects of loading scheme, aspect ratio, concrete strength, and steel ratio on the seismic performance of the CFST specimens were analysed. The longitudinal and the circumferential strains of steel pipes in different stress stages were also investigated to examine the interaction between the steel tube and the core concrete.

2. Experimental Investigation

2.1. Specimen Design and Fabrication. Based on the inclined CFST columns in the Guangzhou International Finance Centre, a model test with the scale principle of the same confinement effect coefficient ξ was conducted, where $\xi = f_y A_s / f_{cm} A_c$, f_y is the yield strength of the steel tube, f_{cm} is the axial compressive strength of the concrete, and A_s and A_c are the cross-sectional areas of the steel tube and the core concrete, respectively. The cross-sectional size of the CFST column is $D \times t = 1800 \times 35$ to 800×20 , which is gradually reduced from the bottom to the upper section. Q345 steel and C60 concrete are selected as materials, and the constraint effect coefficient is between 0.66 and 0.87. To investigate the influence of concrete strength and steel ratio on constraint effect and cyclic response of CFST columns, and referring to the dimensions of the prototype section, the sizes of the scaled section are selected as $D \times t = 140 \times 3.00$ and 133×3.50 , respectively. The steel tubes are made of Q235 steel, the concrete strength grades are C40 and C50, and the calculated constraint coefficient is between 0.63 and 1.01, which includes the variation range of the coefficient in practical projects. Given the differences in the relative magnitude of axial cyclic tension and compression loads on

inclined columns at different stories of the diagrid structure under earthquakes, three typical loading schemes were adopted in this test. Since the aspect ratio of the inclined columns in diagrid structure decreases gradually from the bottom to the top story (ranging from 5.65 to 2.51 for Guangzhou International Finance Centre), the lengths of the inclined columns were taken as 450 mm, 750 mm, and 1000 mm, respectively, and the calculated aspect ratio ranges from 3.01 to 7.14. Therefore, the parameters considered in this test include concrete strength, steel ratio, loading scheme, and aspect ratio. Each parameter considers two to three levels, and then eight CFST columns and two reference hollow steel columns were designed according to orthogonal experimental design method. The specific parameters of the specimens are shown in Table 1.

To facilitate loading and fixation of the specimens in the test, a square steel cover plate with a length of 340 mm is welded at both ends of the steel pipe, a circular hole with a diameter of 90 mm is cut on one side of the cover for concrete pouring, and the geometric centres of the cover plate and the steel pipe are aligned. To avoid damage to the welding seam at the end of the specimen, four stiffeners with a thickness of 8 mm are set between the steel tube and the cover plate on both sides, and the height and length of the rib are both 60 mm with butt welding, as shown in Figure 1. The concrete was poured from the reserved hole at the cover plate. During the pouring and curing period, the specimens were placed upright. After two weeks of natural curing, the floating layer on the top was chiselled and the concrete surface was levelled with the steel pipe with high-strength mortar. All specimens were poured at a time using fine-aggregate commercial concrete. The axial compressive strengths on the day of testing were 51.31 MPa and 60.69 MPa, and the elastic moduli E_c were 29756 N/mm² and 30598 N/mm², respectively. The measured mechanical properties of the two sizes of steel pipes are shown in Table 2.

2.2. Test Setup. As shown in Figure 2, the test uses a self-balanced loading device. The specimen is placed horizontally, and the axial cyclic load is applied through two parallel electrohydraulic actuators connected to the distribution beam through high-strength bolts. To ensure that the specimen is loaded axially, an axially sliding directional is set at the bottom of the connection piece used to connect the distribution beam to the specimens.

In practical engineering, the tension and compression loads of inclined CFST columns often vary greatly at different positions and floors in the structure. Therefore, the loading scheme is considered as a parameter in the test, and the load-displacement hybrid control loading system is selected, which is described as follows.

To facilitate description, we specify that the pushed loading is positive and the pulling loading is negative. The load-control method was used in the initial loading cycles prior to yield. For the hollow steel tube specimen, one cycle was performed for each level with increments of 50 kN in both the positive and negative directions, and the cycle for the CFST specimen was performed for each level with

TABLE 1: Specific parameters of the specimens.

Specimens	D (mm)	t (mm)	f_y (MPa)	f'_c	l_0 (mm)	ξ	Loading procedure
HST-1	140	3	Q235	—	450	—	2
CFST-2	140	3	Q235	C40	450	0.77	1
CFST-3	140	3	Q235	C40	450	0.77	2
CFST-4	140	3	Q235	C40	450	0.77	3
CFST-5	140	3	Q235	C50	450	0.63	2
CFST-6	140	3	Q235	C40	750	0.77	2
CFST-7	140	3	Q235	C40	1000	0.77	2
HST-8	133	3.5	Q235	—	400	—	2
CFST-9	133	3.5	Q235	C40	400	1.01	2
CFST-10	133	3.5	Q235	C50	400	0.83	2

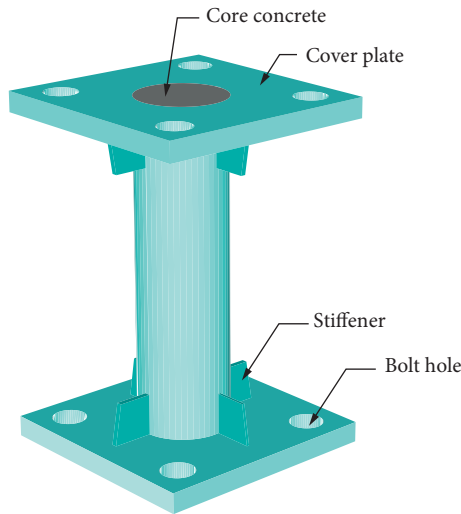


FIGURE 1: Details of the specimen.

TABLE 2: Properties of steel.

$D \times t$ (mm)	E_s/N (mm ²)	f_y (MPa)	f_u (MPa)	δ	μ_s
133 × 3.5	2.07×10^5	324	379	0.21	0.29
140 × 3	1.97×10^5	308	368	0.22	0.29

increments of 100 kN in the positive directions and the 50 kN in negative directions. The different load increments, which were estimated according to the equal strains of the steel tube, were used to ensure that the specimen reached yield simultaneously in both loading directions. After yielding, the loading sequence was controlled by displacement. Three loading systems with three cycles were used in each level with different increments in the test setup.

CFST-2 was subjected to loading system 1 with increments of 0.5 mm in the positive direction and 1 mm in the negative direction, and CFST-4 was subjected to loading system 3 with increments of 1 mm in the positive direction and 0.5 mm in the negative direction. However, CFST-3 was loaded with increments of 0.5 mm in both the positive and negative directions, which was defined as loading system 2, and the other specimens were loaded using loading system 2. The test was terminated when the reaction force descended to approximately 85% of the maximum load or the specimen loading was stopped when it could not withstand the

predetermined axial force. To ensure continuity and uniformity of the cyclic loading, the speed of loading or unloading remained consistent.

2.3. Instrumentation. The test specimens were extensively installed with measuring devices. The axial loads were measured using load cells inside the PM actuators, and the axial deformations were measured using four displacement gauge arranged along the circumferential direction between the two ends of the cover plates. At the same time, the torsional deformation of the test piece could also be monitored. The strain gauge arrangement is shown in Figure 3. In the middle of the steel tube, four three-dimensional strain flowers were arranged along the circumferential direction at the middle of the steel tube, and four two-direction strain flowers were evenly arranged along the circumferential direction at 50 mm from the end of the steel tube. By measuring the longitudinal strain at different positions, the uniformity of axial deformation is considered to determine whether the loading scheme is reasonable. By measuring the transverse strain at different positions, the confinement effect of the steel pipe on the concrete is studied. The oblique strain in the middle of the steel tube is measured to analyse the slip effect on the surface of the steel tube.

3. Specimen Behaviour

3.1. Failure Process. A similar failure process and failure mode were observed for eight CFST specimens, which all experienced six stages as follows: concrete cracking, concrete crushing, steel tube external drum, steel tube cracking, local buckling of steel tube, and steel tube fracture. At the beginning of loading, the concrete is cracked under tension. After the concrete cracks, the tensile bearing capacity of the specimen continues to increase. At this time, the steel pipe plays a major role and the concrete mainly plays a supporting role. When the concrete is compressed to crushing, the concrete is in a three-directional force state based on the restraint of the steel tube, and the compression bearing capacity continues to increase. When the specimen puffs out and peels, the vertical pressure between the steel tube and concrete is redistributed. The compressed pressure sustained by the steel pipe continues to decrease while the concrete supplies higher compressive strength due to the

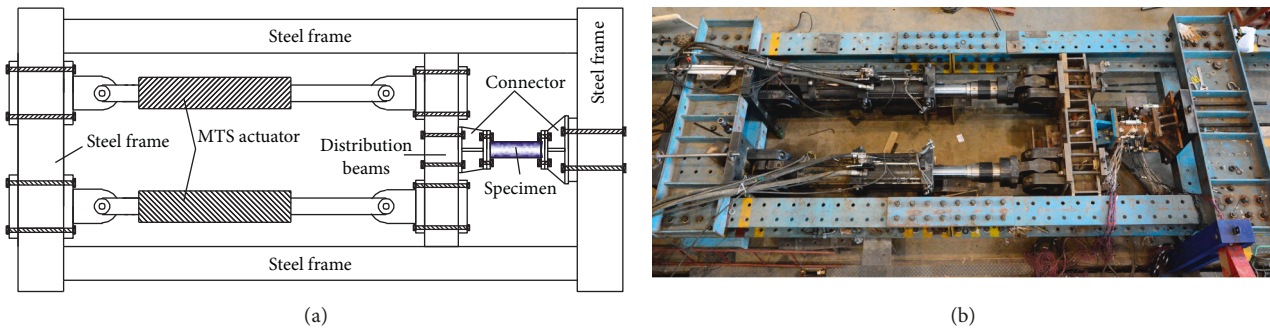


FIGURE 2: Test setup: (a) diagram of the loading device; (b) photograph of the loading device.

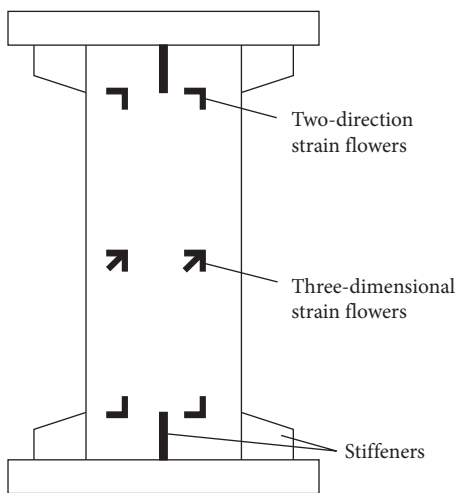


FIGURE 3: Measurement of steel tube strain.

circumferential restraint of the steel pipe. The specimen reaches peak load capacity in the compression direction when the sum of the longitudinal pressures received by the concrete and the steel tube reaches a maximum. Subsequently, the end of the steel pipe cracks and reaches the peak bearing force in the tension direction. Eventually, the steel pipe displays local cracking at the cracking end of the steel pipe, which means that the compressive bearing capacity of the specimen begins to decrease rapidly. Finally, the steel pipe at buckling shows tensile fracture in the reverse cycle, and the specimen loses its bearing capacity. The failure process of two hollow steel pipe column specimens is similar to that of concrete-filled steel tubular column specimens under cyclic load. All specimens experienced four stages: steel tube peeling, steel tube cracking, steel tube local buckling, and steel tube fracture. However, the number of the cycles that the hollow steel tube experienced is less than that of the CFST specimens, and the failure process of the HST specimens is more rapid than that of the CFST specimens. The final failure modes of all ten specimens are shown in Figure 4.

3.2. Analysis of Failure Characteristics. The diameter-thickness ratio of the steel tube, the aspect ratio of the specimen, and the loading scheme all have effects on the

cracking and local buckling of the steel tube. Local buckling and cracking of the steel tube occur easily if the diameter-thickness ratio is larger, local buckling of the steel pipe occurs easily if aspect ratio of the specimen is larger, and the steel pipe experiences different damage conditions under different loading schemes. Specifically, CFST-2 with larger incremental displacement in the tensile direction experiences the least cycles when the steel pipe cracks. CFST-4 with a larger incremental displacement in the compressive direction experiences the least cycles when the steel tube buckles. CFST-3 experiences more cycles whenever the steel tube cracks or buckles for smaller incremental displacements in both compressive and tensile directions, but the failure displacement of the CFST-3 specimen is the smallest.

To observe the damage of the core concrete, three specimens with different geometrical dimensions were selected for peel off of the outer steel pipe after the test. The crack distribution and failure mode of the core concrete are shown in Figure 5. It can be observed that the core concrete remains intact, and concrete crushing occurs only at the buckling position of the steel pipe, which is located near the end of the specimen. In particular, the CFST-5 specimen displays greater brittleness, the concrete crushing is the most significantly for higher concrete strength, and CFST-5 is completely broken after the external steel pipe is stripped out. The core concrete of each specimen exhibits multiple parallel and unequally spaced cracks, with a small number of longitudinal cracks and no oblique cracks. The results verified that all specimens are axially loaded, with no occurrence of torsion and eccentricity.

4. Experimental Results

4.1. Hysteretic Behaviour. The hysteresis responses of ten specimens are plotted in Figure 6. The characteristics of the hysteresis curves are discussed in the following.

The hysteresis curves of the CFST specimens are full under an axial cyclic load, showing better deformability and energy dissipation capacity. At the initial stage of loading, the hysteresis curves are narrow and slender, and the surrounding area of the hysteresis loop is small. The stiffness of the specimens has not obviously changed, and the residual deformation is quite small. After the specimens have yielded, cracking of the concrete is intensified, the steel pipe displays cracking and peeling, the surrounding area of the hysteresis

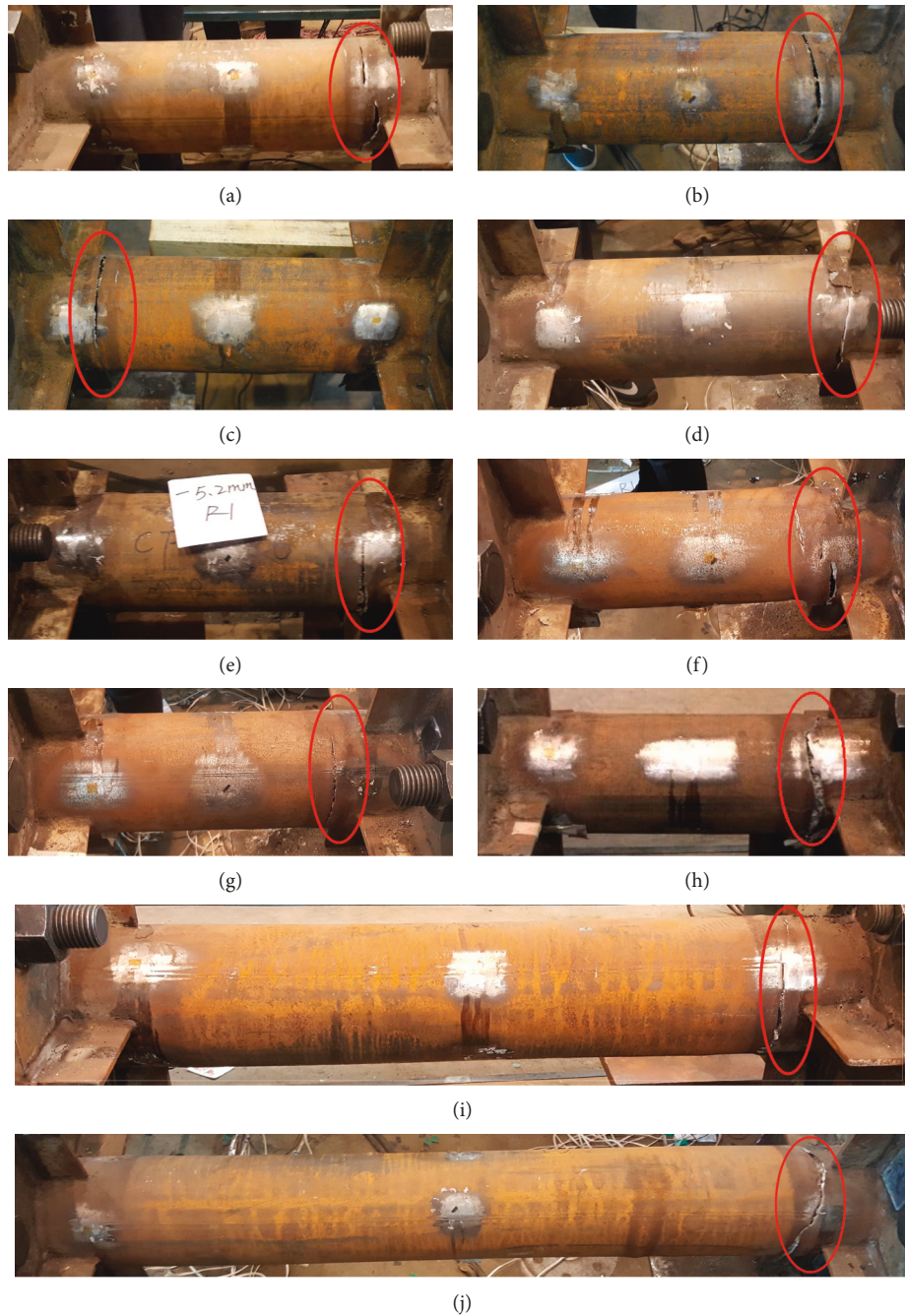


FIGURE 4: Specimens in failure. (a) HST-1; (b) CFST-2; (c) CFST-3; (d) CFST-4; (e) CFST-5; (f) HST-8; (g) CFST-9; (h) CFST-10; (i) CFST-6; (j) CFST-7.

loop begins to increase, the energy dissipation capacity increases, the stiffness of the specimens begins to gradually degenerate, and residual deformation appears. After reaching the peak load, the specimen can still continue to supply a stable bearing capacity. With the increase in the crack width of the concrete and the local buckling of the steel tube, the specimen shows a certain “pinching effect.” Under cyclic load, due to accumulation of damage, the specimen exhibits obvious strength degradation and stiffness degradation in the same stage of the displacement cycle, and the energy dissipation capacity is weakened.

Due to the anisotropy of concrete, the stress mechanism of the CFST specimens shows significant differences between the axial compression direction and the axial tension direction, and thus the hysteresis loops show obvious asymmetry and exhibit different characteristics in the directions of tension and compression. In general, when CFST columns are subjected to tension, the concrete plays a supporting role for the steel tubes, inhibits necking of the tubes, and makes the hysteresis loop more full, which ensures the good deformation and energy dissipation capacities of the specimen in the tension direction. When the concrete-filled steel tube

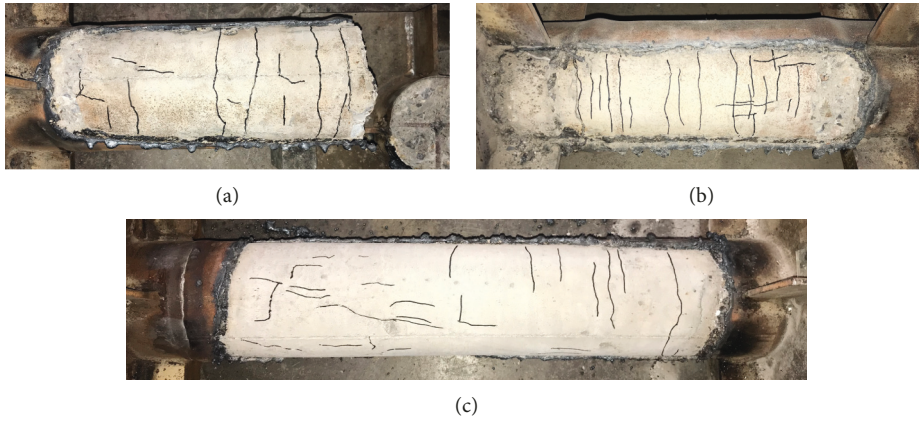


FIGURE 5: Core concrete in failure. (a) CFST-5; (b) CDST-10; (c) CFST-6.

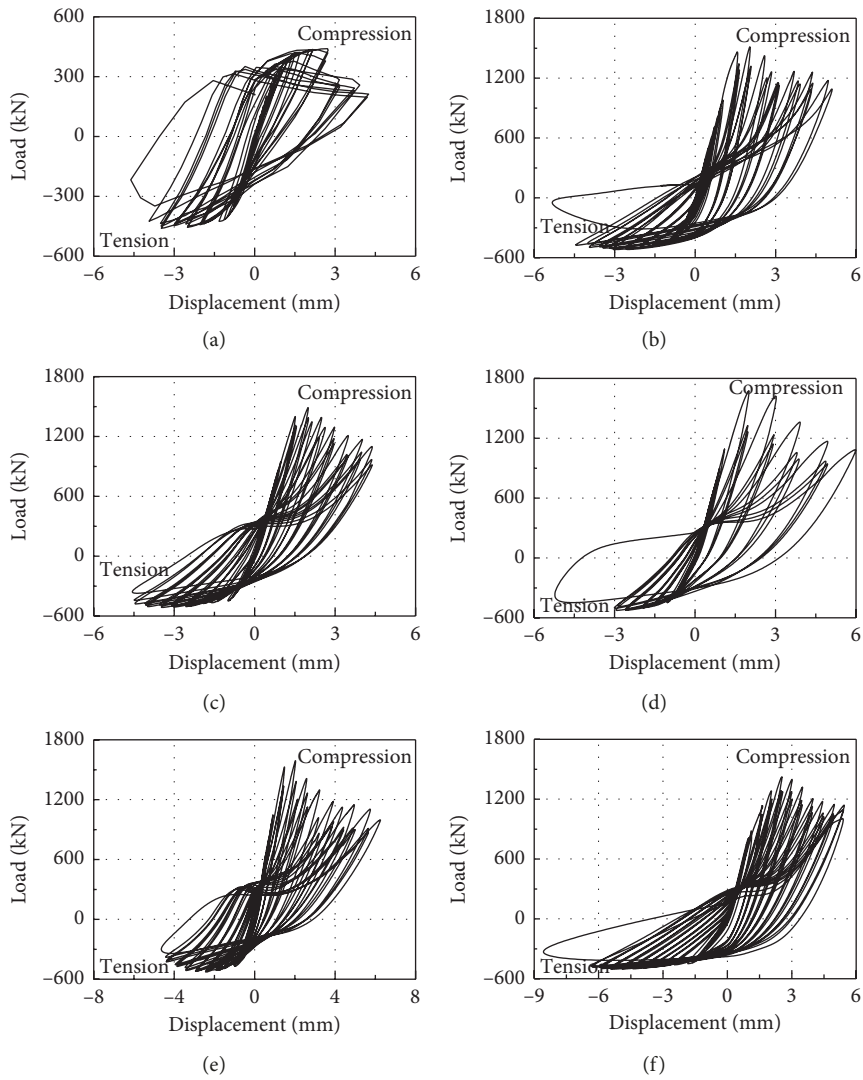


FIGURE 6: Continued.

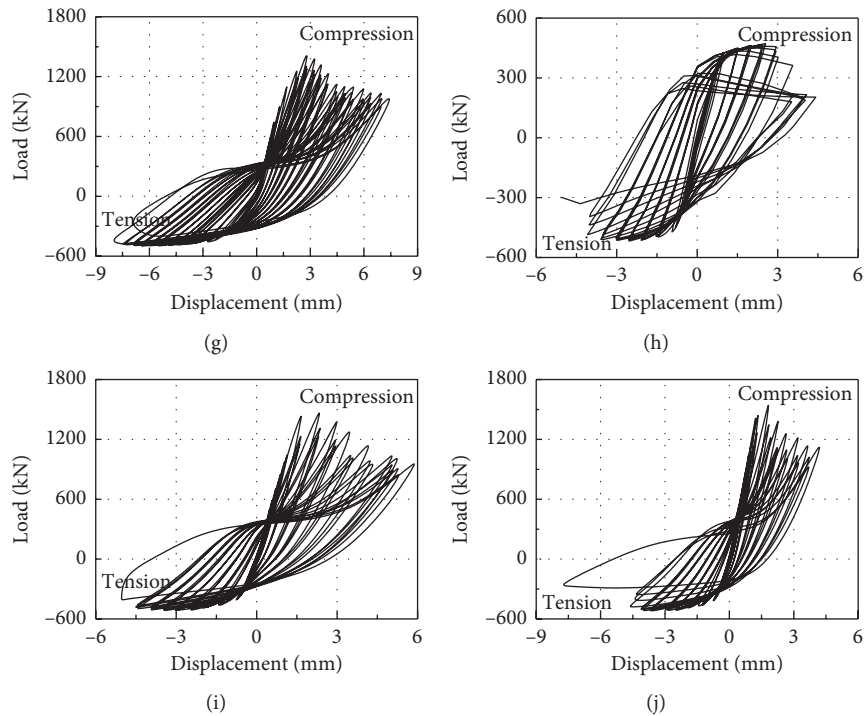


FIGURE 6: Cyclic axial load versus longitudinal deformation curves for specimens. (a) HST-1; (b) CFST-2; (c) CFST-3; (d) CFST-4; (e) CFST-5; (f) CFST-6; (g) CFST-7; (h) HST-8; (i) CFST-9; (j) CFST-10.

column is placed under pressure, although the restraint of the steel tube on the concrete and the concrete inhibition of buckling of the steel tube both enhance the deformation capacity of the CFST specimens to a certain extent, the load-carrying capacity of the specimens decreases rapidly after the concrete crushing and the local buckling of the steel tube appear. Compared with the tension direction, the energy dissipation capacity is relatively weaker in the compressive direction.

The pinching effect was quite obvious when the CFST specimens were transferred from the tension state to the compression state, which results from the large number of cracks with greater width as well as the obvious bond-slip between the steel tube and the core concrete. Obvious crack closure occurs when the load is reversed, which contributes an obvious pinching phenomenon. However, the hysteresis curve of the CFST specimen shows a minimal pinching phenomenon when the specimen is transferred from the compression to the tension state. The result is that no obvious cracking occurs in the compression of the concrete, no obvious bond slip is observed between the steel tube and the core concrete, and thus no crack closure occurs when the load is reversed.

By comparing the specimens under different loading schemes, it can be observed that the pinching effect of CFST-2 is the most significant, followed by the CFST-3 specimen, and the hysteretic curve of CFST-4 is the fullest due to the larger increment of the tensile displacement of CFST-2, the rapid cracking of the concrete, and the rapid expansion of the crack. The slip between the steel pipe and the concrete is also more pronounced, and thus the

pinching effect of CFST-2 is the most significant when the load is reversed. The displacement increment of CFST-4 in the compressive direction is larger, and the deformation capacity and the bearing capacity are higher. Therefore, CFST-4 has a greater energy dissipation capacity. When the concrete strength increases, the bearing capacity of the specimen increases, the pinching effect of the hysteresis curve is intensified, and the strength and stiffness degeneration are more significant. As the steel ratio increases, the hysteretic curve of the specimen becomes plumper and the deformation capacity and energy dissipation capacity are stronger. As the aspect ratio increases, the deformability of the specimen increases, the bearing capacity slightly decreases, and the energy dissipation capacity increases. Compared with the CFST specimens, the hysteresis curve of the hollow steel tube specimens is plumper, with no pinching phenomenon.

4.2. Envelope Curves. Figure 7 plots the envelope curves for the specimens under different parameters. It can be observed that the skeleton curves of the CFST specimens show different characteristics in the tensile and compressive directions.

When the CFST specimen is compressed, the steel tube and concrete both participate in the work, but only the steel tube is involved in the force when the specimen is under tension. Therefore, the bearing force in the compression direction is far greater than in the tension direction. At the same time, the deformability in the compression direction is far less than the deformability in the tension direction

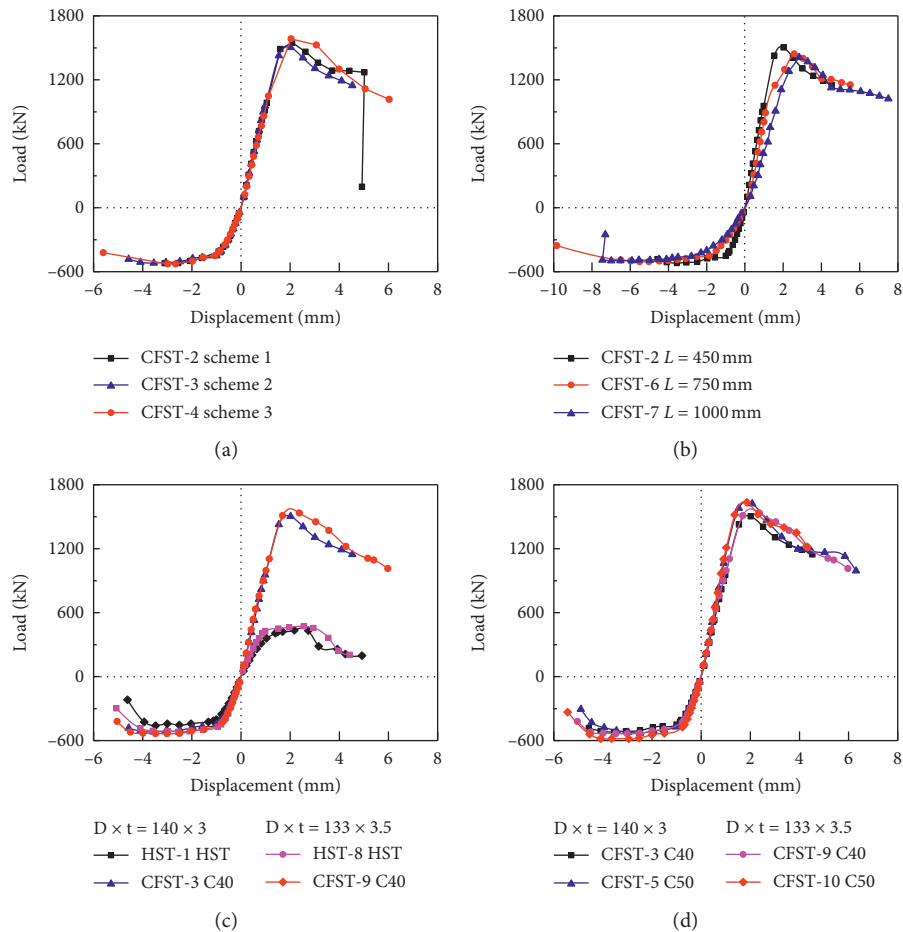


FIGURE 7: Envelope curves of specimens.

because the core concrete can effectively restrain the necking of the steel tube and delay the failure of the specimen in the tensile direction. In contrast, the local buckling of the steel pipe is accelerated by the core concrete and leads to failure of the CFST specimens in the compression direction, especially after the steel pipe is cracked. For hollow steel tube specimens, the bearing capacity is similar in the compression and tension directions, but the deformation ability in the compression direction is still far smaller than that in the tension direction.

Figure 7(a) shows that the skeleton curves of the CFST specimens nearly coincide in the tensile direction under different loading schemes because the loading schemes have little effect on the damage to the steel tube, which mainly determine the bearing capacity and the deformability of the CFST specimens. In the compression direction, the CFST-4 specimen with the least number of cycles has the highest bearing capacity, whereas the CFST-3 specimen with the largest number of cycles has the lowest bearing capacity, and the bearing capacity of CFST-2 falls in the middle.

Figure 7(b) shows that the bearing capacity of the specimens decreases slightly with increasing aspect ratio, which further verifies that the specimens were loaded concentrically. At the same time, the deformability of the specimen increases with increasing aspect ratio, but the

displacement ductility decreases, and the strength attenuation is more obvious after the peak load.

In Figure 7(c), it can be observed that the bearing capacity and deformability of the CFST specimens are slightly higher than those of the hollow steel tube specimens in the tension direction due to the supporting effect of concrete on the steel pipe, which can restrain and delay the necking of the steel tube to a certain extent. In the compression direction of the specimen, the bearing capacity and deformability of the CFST specimens are significantly higher than those of the hollow steel tube specimen, which shows that both the concrete and the steel tube are involved in the compression and that the concrete can restrain the local buckling of the steel tube to a certain extent, but no obvious yielding platform appears for the CFST specimens.

Figure 7(d) shows that the concrete strength has little effect on the skeleton curve in the tension direction of the specimen, whereas the rigidity of the specimen and the bearing capacity both increase with increasing concrete strength in the compression direction. Moreover, the ductility decreases with increasing strength of the concrete.

Figures 7(c) and 7(d) show that the bearing capacity and the deformability of all specimens are increased with the increasing steel ratio in the tension direction. In the

compression direction, the bearing capacity of the two cross-sectional dimensions (calculated by simply superimposing the cross-sectional area and the material properties of the steel and concrete) is equivalent, but the bearing capacity and the deformability of the larger steel ratio specimen with a larger confinement factor are greater.

4.3. Ductility. The displacement ductility coefficient is used to express the deformation capacity of the specimens, which is defined as the ratio of the ultimate displacement Δ_{\max} to the yield displacement Δ_y , namely, $\mu = \Delta_{\max}/\Delta_y$. The ultimate displacement is defined as the displacement when the bearing capacity is reduced to 85% of the peak load, and the yield displacement is determined based on the energy equivalence method. The measured results, such as yield load, peak load, ultimate load, and the corresponding displacements as well as the displacement ductility coefficients for each specimen, are summarised in Table 3.

It can be observed that the yield displacements are similar under the directions of tension and compression, but the yield load in the tensile direction is only 1/3 of that in the compression direction for CFST specimens, indicating that the elastic stiffness in the compression direction is significantly greater than that in the tension direction.

The peak bearing capacity of each specimen under compression direction is 2.74–3.19 times that under the tension direction, but the ultimate displacement under the compression direction reached only 49–80% of that under the tension direction, indicating that the core concrete not only contributes greatly to the compression bearing capacity of the CFST specimens but also delays the tensile failure.

The yield load, yield displacement and peak load of the hollow steel specimen are generally similar in the tension and compression directions. However, the ultimate displacement under the compression direction is only 70% of that under the tension direction, which indicates that the tension cracking of the steel tube accelerates the buckling of the steel pipe. The ductility coefficient of the specimens is 1.63–3.44 in the compression direction, and the ductility coefficient is 3.11–5.45 in the tension direction, showing good ductility overall.

The loading scheme has a significant influence on the bearing capacity but has little effect on the displacement ductility. With the increase in the aspect ratio, the ductility of the specimen is gradually decreased. Although the ultimate deformability of the CFST specimens in the compression direction is better than that of the hollow steel tube specimens, the displacement ductility of the specimens is slightly smaller than that of the hollow steel specimens due to the large yield displacement of the CFST specimens. In the tension direction, the ultimate deformability and the displacement ductility of the CFST specimens are better than those of the hollow steel tube specimens. At the same time, the concrete strength has little effect on the ductility of the specimen in the tension direction because the destruction of the specimen is controlled by the steel tube, whereas the concrete only plays a supporting role.

5. Strain Analysis

At the stress-strain level, the longitudinal strain gauges can be used to investigate the uniformity of the axial deformation of the specimen, and the transverse strain gauges were placed to obtain the transverse/longitudinal strain ratio to gather evidence of the confining effects. The interaction effect between the steel tube and the core concrete can be analysed using Poisson's ratio ν_{sc} . Poisson's ratio ν_{sc} of the composite material is defined as the ratio of the absolute value of the transverse strain to the longitudinal strain of the steel pipe, values that are obtained from the steel tube strain gauges. Poisson's ratio of the steel is 0.3. Therefore, it is considered that the steel tube has a transverse effect on the core concrete when Poisson's ratio of the composite materials exceeds 0.3. Therefore, the restraining effect of the steel tube on the concrete is analysed using the variation law of ν_{sc} in this paper.

Figure 8 shows the longitudinal strain distribution of HST-1, and the longitudinal strain of the specimen is approximately equal for each section, thus verifying that the specimens were loaded axially and uniformly. The average value of the longitudinal strain at four measuring points is analysed in the following study.

5.1. Restraint Effect of HST and CFST in the Tension and Compression Directions. For the hollow steel tube, the $|\varepsilon_{s,t}/\varepsilon_{s,l}|$ ratio is expected to be approximately equal to Poisson's ratio ν_s , which is generally taken as 0.3 for the steel material. The $|\varepsilon_{s,t}/\varepsilon_{s,l}|$ ratio versus the axial load and the $|\varepsilon_{s,t}/\varepsilon_{s,l}|$ ratio versus the average longitudinal strain for all twelve measuring points of the hollow steel specimen HST-1 are plotted in Figure 9. These figures show that the ratios are generally stable at 0.3 as the load increases. The hollow steel tube is considered to be in the uniaxial stress state and is able to shrink and bulge freely without the core concrete. However, the compression deformation of the steel tube cannot be flattened with the development of the plastic deformation, the residual bulging phenomenon still appears in the tension direction, and the $|\varepsilon_{s,t}/\varepsilon_{s,l}|$ ratio decreases at first and subsequently increases.

When the CFST specimen is under tension, we can assume the biaxial stress state for the steel tube element. Although the circumferential stress due to the confinement of concrete can be neglected in the tension direction, the transverse stress caused by the constraint of the concrete and its influence on the $|\varepsilon_{s,t}/\varepsilon_{s,l}|$ ratio cannot be ignored. When the CFST specimens are subjected to axial tension, the shrinkage of the steel tube is supported by the concrete, which leads to the negative radial reaction force of the steel tube. With the increase in the axial tension, the $|\varepsilon_{s,t}/\varepsilon_{s,l}|$ ratio gradually decreases, but the $|\varepsilon_{s,t}/\varepsilon_{s,l}|$ ratio begins to increase at the later stage of loading, which results from the residual bulge deformation caused by the large plastic compressive deformation. Figure 10 plots the $|\varepsilon_{s,t}/\varepsilon_{s,l}|$ ratio versus axial load and the $|\varepsilon_{s,t}/\varepsilon_{s,l}|$ ratio versus average longitudinal strain for the twelve measuring points of CFST-3. These figures show that the ratios decrease with an increase in

TABLE 3: Experimental results.

Specimens	Direction	Yield		Peak		Ultimate		μ
		P_y (kN)	Δ_y (mm)	P_p (kN)	Δ_p (mm)	P_u (kN)	Δ_u (mm)	
HST-1	Compression	376.77	1.16	435.99	2.17	370.59	2.92	2.52
	Tension	-400.18	-1.00	-459.88	-3.48	-390.90	-4.05	4.05
CFST-2	Compression	1504.34	1.73	1549.62	2.08	1317.18	3.47	2.01
	Tension	-423.47	-1.05	-520.77	-4.70	-442.66	-4.48	4.27
CFST-3	Compression	1435.00	1.60	1504.00	2.02	1278.40	3.24	2.03
	Tension	-451.05	-1.02	-518.75	-3.55	-440.93	-4.57	4.48
CFST-4	Compression	1490.00	1.88	1684.08	2.04	1431.47	3.80	2.02
	Tension	-450.67	-1.07	-527.59	-2.66	-448.46	-4.94	4.62
CFST-5	Compression	1584.00	1.51	1622.56	2.07	1379.17	3.02	2.00
	Tension	-458.78	-0.98	-530.32	-2.79	-450.77	-4.24	4.33
CFST-6	Compression	1315.00	2.10	1443.29	2.58	1226.80	3.94	1.88
	Tension	-439.68	-1.79	-505.93	-5.02	-430.04	-8.00	4.47
CFST-7	Compression	1362.26	2.60	1409.79	2.84	1198.32	4.24	1.63
	Tension	-424.52	-2.28	-497.96	-6.99	-423.27	-7.08	3.11
HST-8	Compression	-451.98	0.96	471.77	2.61	-439.70	3.31	3.44
	Tension	-451.98	-0.82	-517.30	-2.55	-439.70	-4.33	5.28
CFST-9	Compression	1507.92	1.68	1535.50	2.38	1305.18	3.89	2.32
	Tension	-440.49	-0.89	-560.00	-2.51	-476.00	-4.85	5.45
CFST-10	Compression	1565.46	1.57	1634.76	1.86	1389.55	3.48	2.22
	Tension	-481.89	-0.88	-583.41	-2.53	-495.90	-4.73	5.38

the tension loading. It can be observed that the $|\varepsilon_{s,t}/\varepsilon_{s,l}|$ ratio is stable at 0.3 prior to cracking. This result indicates that the concrete has not completely restricted the tube initially before the cracking of the concrete because the specimen is under an elastically tension load and the diameter decreases due to the Poisson effect. But the restraint effect still occurs in the concrete-filled steel tube members because of the difference of Poisson's ratio between steel tube and core concrete, which makes the core concrete play a supporting role. After concrete cracking, the concrete is partially unloaded, which shows a more significant supporting effect on the external steel tube. At the later stage of loading, the steel tube cracks and plastic deformation of the outer drum occur under the following compression loading, the transverse strain decreases gradually, and the $|\varepsilon_{s,t}/\varepsilon_{s,l}|$ ratio decreases.

When the specimen is compressed, the steel tube has a transverse restraint effect on the core concrete. At first, the steel tube and the concrete are in an elastic stress state without the restraint effect, and the $|\varepsilon_{s,t}/\varepsilon_{s,l}|$ ratio is stable at 0.3. As the concrete is crushed, the steel tube begins to restrain the concrete, and the $|\varepsilon_{s,t}/\varepsilon_{s,l}|$ ratio increases, as shown in Figure 10, which plots the $|\varepsilon_{s,t}/\varepsilon_{s,l}|$ ratio versus axial load and the $|\varepsilon_{s,t}/\varepsilon_{s,l}|$ ratio versus average longitudinal strain of CFST-3. It can be observed that the $|\varepsilon_{s,t}/\varepsilon_{s,l}|$ ratio is stable at 0.3 before the concrete is crushed. With crushing of concrete, the transverse strain of the concrete becomes gradually greater than that of the steel tube. The steel tube begins to restrain the concrete, and the $|\varepsilon_{s,t}/\varepsilon_{s,l}|$ ratio increases gradually, which also appears in the later period of tensile test.

Figure 10 shows that the strains of the four measuring points of the same section are approximately equal, indicating that the restraining effect is evenly distributed in the same section.

5.2. Parameter Analysis of the Constraint Effect in the Compression Direction. Figure 11 plots the $|\varepsilon_{s,t}/\varepsilon_{s,l}|$ ratio versus axial load, showing that the $|\varepsilon_{s,t}/\varepsilon_{s,l}|$ ratio is generally maintained at approximately 0.3 initially because the steel pipe has not yet formed an effective constraint on the concrete. When the axial load is between the proportional limit and the yield load, the $|\varepsilon_{s,t}/\varepsilon_{s,l}|$ ratio increases slowly as the core concrete is gradually crushed and the steel tube begins to constrain the concrete. The $|\varepsilon_{s,t}/\varepsilon_{s,l}|$ ratio increases sharply when the specimen is loaded from the yield point to the peak load. After the peak load is reached, the $|\varepsilon_{s,t}/\varepsilon_{s,l}|$ ratio continues to increase while the bearing capacity begins to decrease, and the restraint effect continues to increase, resulting in better holding capacity. Figure 12 plots the transverse strain versus the restraint coefficient and the transverse strain versus aspect ratio at the same longitudinal strain. As shown in Figure 12(a), the corresponding transverse strains of the specimens with different aspect ratios are nearly equal when the longitudinal strain reaches $1500 \mu\varepsilon$ because the steel tube has not completely yielded, the concrete has not cracked, and the constraint effect cannot yet be realised. The corresponding transverse strain of the specimen with a larger aspect ratio is slightly smaller when the longitudinal strain reaches $3000 \mu\varepsilon$ and $6000 \mu\varepsilon$. When the longitudinal strain reaches $8000 \mu\varepsilon$, the circumferential strain of CFST-3 is $6206 \mu\varepsilon$, and the transverse strains of CFST-6 and CFST-7 are $4960 \mu\varepsilon$ and $4440 \mu\varepsilon$, showing that the difference of the circumferential strain with different aspects is further enlarged. When the longitudinal strain reaches $10000 \mu\varepsilon$, the corresponding transverse strain of CFST-3 is $8240 \mu\varepsilon$ and those of CFST-6 and CFST-7 are $7200 \mu\varepsilon$ and $6500 \mu\varepsilon$. In general, the confinement effect of the steel pipe on the concrete gradually weakens with the increase in aspect ratio, and the effect of the

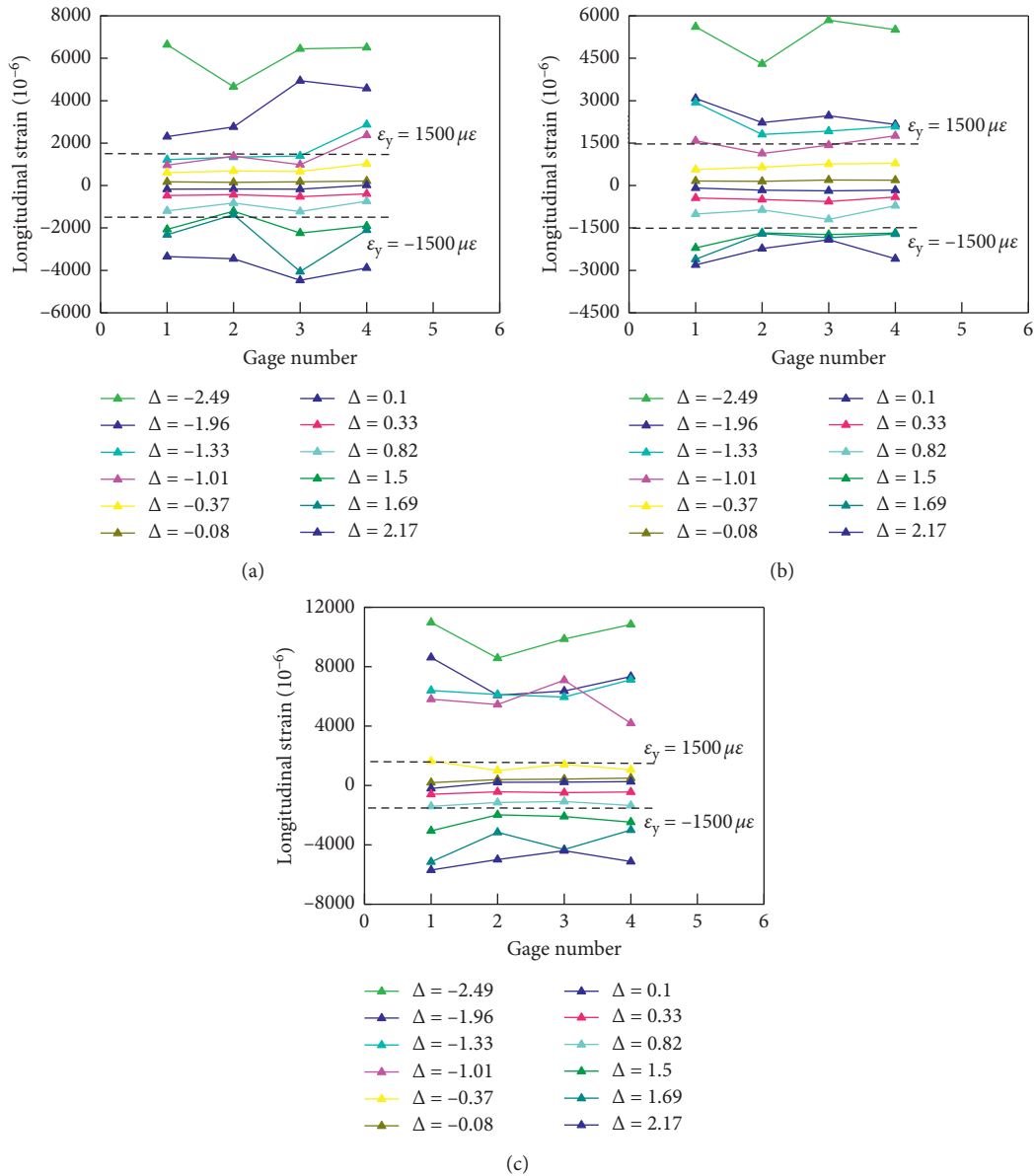


FIGURE 8: Longitudinal strain. (a) Loading end; (b) constraint end; (c) central section of the column.

length-diameter ratio becomes more significant with the increase in longitudinal strain with a certain range.

From Figure 12(b), it can be observed that the transverse strains of the specimens with different restraining coefficients are generally equal. Although the transverse strain of the specimen with a larger restraining coefficient is slightly larger when the longitudinal strain reaches $3000 \mu\epsilon$, at this time, the concrete is cracked but not crushed, which means that Poisson's ratio of the concrete increases slightly and the constraint effect begins to appear. When the longitudinal strain reaches $6000 \mu\epsilon$, the corresponding transverse strains of CFST-3 and CFST-5 are $4098 \mu\epsilon$ and $3670 \mu\epsilon$, and the corresponding transverse strains of CFST-9 and CFST-10 are $4772 \mu\epsilon$ and $3792 \mu\epsilon$, respectively. When the longitudinal strain reaches $8000 \mu\epsilon$, the corresponding transverse strains of CFST-3 and CFST-5 are $6306 \mu\epsilon$ and

$5792 \mu\epsilon$, and the transverse strains of CFST-9 and CFST-10 are $6923 \mu\epsilon$ and $6040 \mu\epsilon$, respectively. The transverse strain increases, and the confinement of the steel tube is obviously improved with the increase in the restraint effect coefficient when the longitudinal strain reaches $6000 \mu\epsilon$ and $8000 \mu\epsilon$. When the longitudinal strain reaches $10000 \mu\epsilon$, the transverse strains of the specimens under different confinement coefficients are similar because the steel tube has buckled in the compressive direction and no longer supplies the constraint force on the concrete, and thus the constraint effect reaches the maximum at this time.

6. Conclusions

In this paper, an experimental programme was conducted on eight CFST specimens and two hollow steel tube

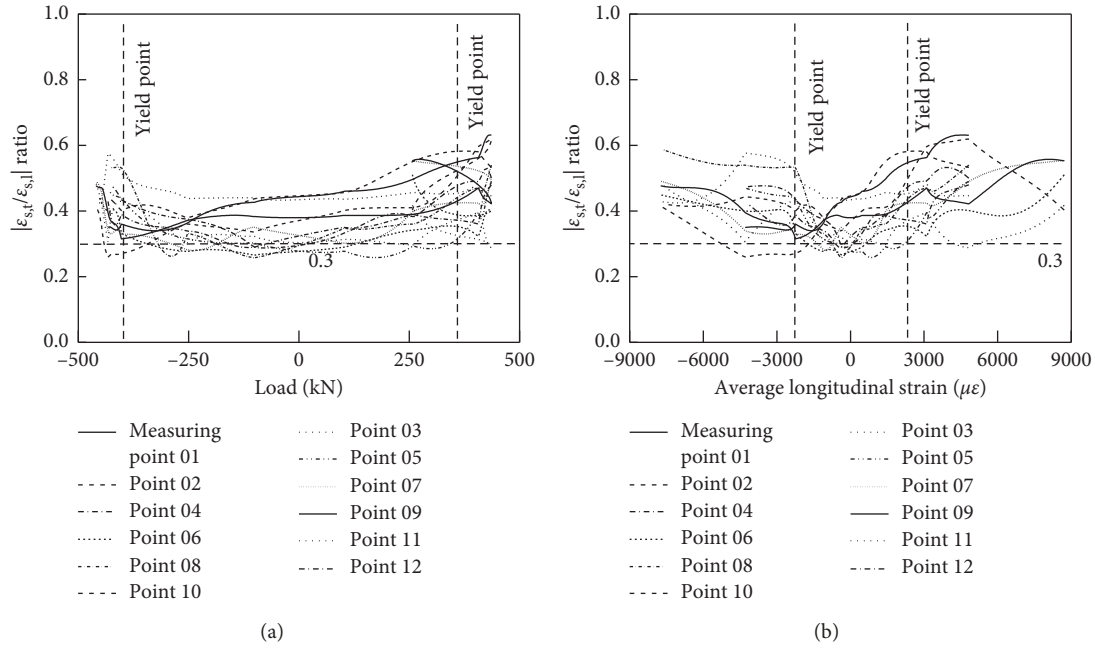


FIGURE 9: $|\varepsilon_{s,t}/\varepsilon_{s,l}|$ ratio variation of HST-1. (a) $|\varepsilon_{s,t}/\varepsilon_{s,l}|$ ratio versus average axial load; (b) $|\varepsilon_{s,t}/\varepsilon_{s,l}|$ ratio versus average longitudinal strain.

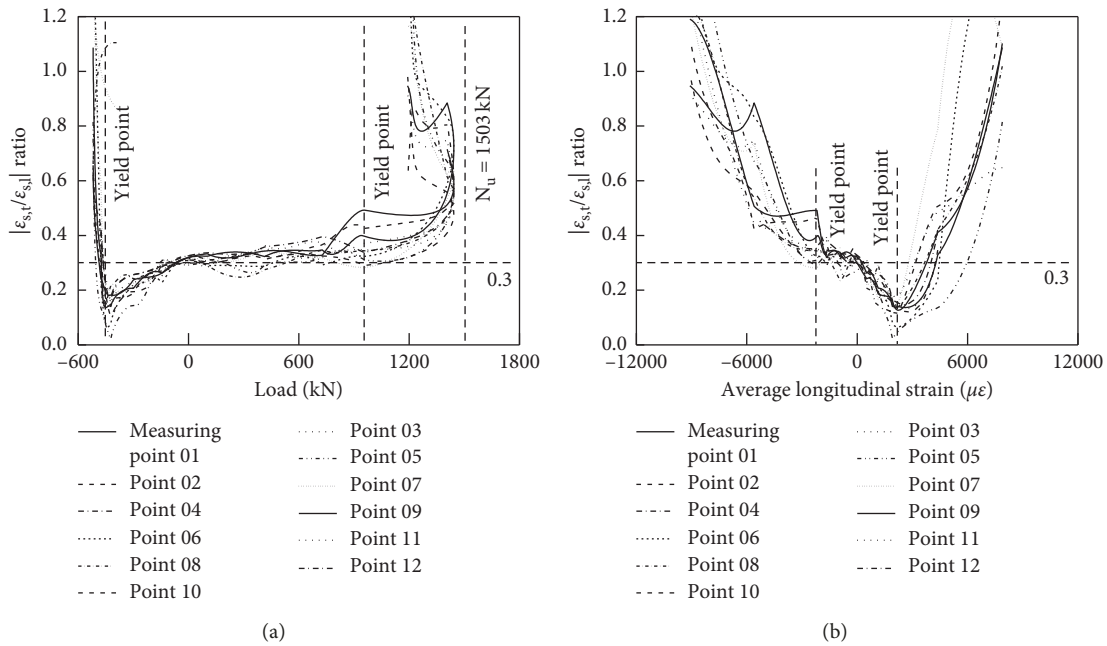


FIGURE 10: $|\varepsilon_{s,t}/\varepsilon_{s,l}|$ ratio variation of CFST-3. (a) $|\varepsilon_{s,t}/\varepsilon_{s,l}|$ ratio versus average axial load; (b) $|\varepsilon_{s,t}/\varepsilon_{s,l}|$ ratio versus average longitudinal strain.

specimens under cyclic axial loads. The results of the specimens were discussed in terms of failure characteristics, hysteresis behaviours, and ductility. The following conclusions can be drawn:

- (1) The eight CFST specimens failed after experiencing six stages of concrete cracking, concrete crushing, steel tube drum, steel tube cracking, local buckling of

steel tubes, and steel tube failure. Two hollow steel tube specimens were subjected to steel tube peeling, steel tube cracking, local buckling of steel tubes, and fracture of the steel tubes in four stages. The failures of all specimens were caused by the end of steel pipe fracture, whereas concrete crushing occurred only at the buckling point of the steel tube, and the core concrete remained intact.

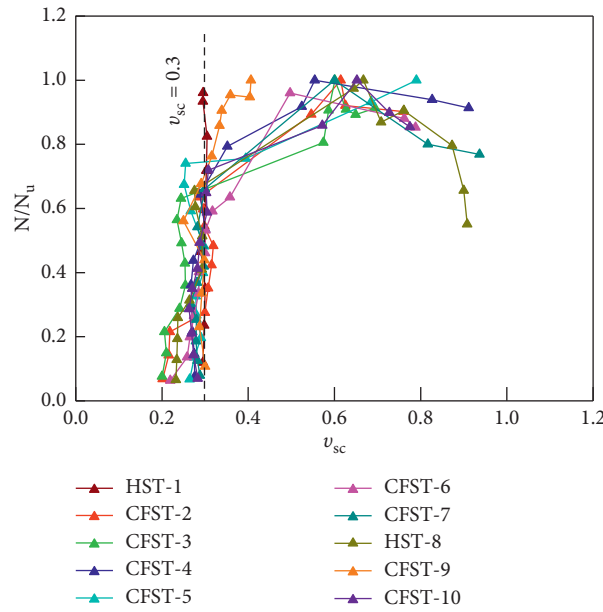


FIGURE 11: Poisson's ratio of composite material load curves.

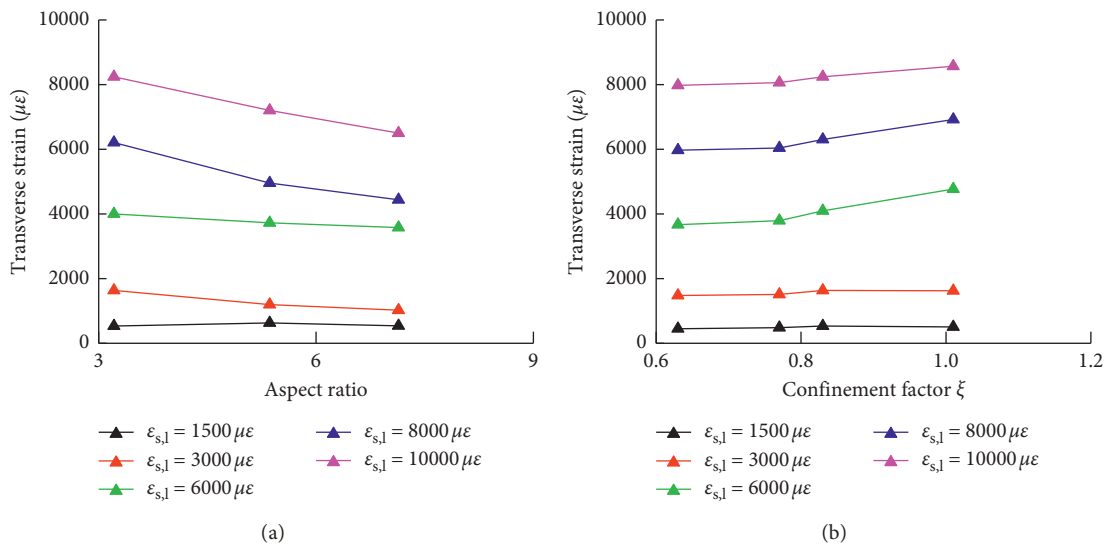


FIGURE 12: Transverse strain variation of CFST-3. (a) Transverse strain versus aspect ratio; (b) transverse strain versus confinement factor.

- (2) The seismic behaviour of CFST columns is significantly different under axial compression loads and axial tensile loads, which show better ductility and energy dissipation in the tension direction and higher bearing capacity and larger stiffness in the compression direction.
- (3) Compared with the hollow steel tube specimens, the CFST specimens have higher bearing capacity and better deformation capacity due to the supporting effect of the concrete on the steel tube in the tension direction and the restraint effect of the steel pipe on the concrete in the compression direction.
- (4) Under different loading schemes, the steel tube of the specimen with a larger increment in the tension

direction is easier to crack and the energy dissipation capacity is better. However, the specimen with a larger increment in the compression direction is easier to buckle, has a higher bearing capacity, and shows slower stiffness degradation. With the increase in aspect ratio, the energy dissipation capacity of the specimen increases, but the bearing capacity and ductility decrease. With the increase in concrete strength, the bearing capacity of the specimen increases and the degradation of strength and stiffness becomes more serious, but the influence on ductility and energy dissipation capacity is not obvious. With increasing steel content, the specimen bearing capacity, deformation capacity, and energy dissipation capacity are correspondingly improved.

- (5) The constraint mechanism shows a significant difference in the compression direction and tension direction, whereas core concrete acts as a brace to resist the steel tube shrinkage and the steel tube restrains the core concrete in compression. In tension direction, the ratios decrease with an increase in the tension loading. In compression direction, $|\varepsilon_{s,t}/\varepsilon_{s,l}|$ ratio increases nonlinearly after yielding of the CFST columns, and the maximum value can exceed 1. This result shows that the constraint effect continues to increase after peak load, enabling the specimens maintain a good load-bearing capacity. The influence of different parameters on the restraining effect reaches a maximum when the longitudinal strain of the steel tube reaches $8000 \mu\varepsilon$.

Data Availability

The data used to support the findings of this study are included within the article.

Conflicts of Interest

The authors declare that there are no conflicts of interest regarding the publication of this paper.

Acknowledgments

The authors would like to express deep gratitude to the laboratory staff and graduate students of the Xi'an University of Architecture and Technology for their help with construction and testing of the specimens. The work was supported by the National Natural Science Foundation of China (Grant nos. 51478382 and 51808435) and China Postdoctoral Science Foundation (Grant no. 2018M643594) Major State Key Research Development Foundation of China (Grant no. 2017YFC0703400).

References

- [1] J. Lee, J. Kong, and J. Kim, "Seismic performance evaluation of steel diagrid buildings," *International Journal of Steel Structures*, vol. 18, no. 3, pp. 1035–1047, 2018.
- [2] J. Zhou and D. Wang, "Performance research on high-rise diagonal frame structure," *Building Structure*, vol. 37, no. 5, pp. 87–91, 2007.
- [3] F. Zhao, *The Basic Study of Mechanical Properties on Diagrid Tube Structure System for High-Rise Buildings*, Tsinghua University, Beijing, China, 2012.
- [4] W. Guo, *Mechanical Performance and Seismic Failure Control Research on High-Rise Diagrid Tube Structures*, Harbin Institute of Technology, Harbin, China, 2011.
- [5] W. Zhou, J. Zhang, and Z. Cao, "Experiment and analysis on X-shaped reinforced concrete joint in diagrid structures," *ACI Structural Journal*, vol. 110, no. 2, pp. 171–182, 2013.
- [6] Y.-J. Kim, M.-H. Kim, I.-Y. Jung, Y. K. Ju, and S.-D. Kim, "Experimental investigation of the cyclic behavior of nodes in diagrid structures," *Engineering Structures*, vol. 33, no. 7, pp. 2134–2144, 2011.
- [7] X. Han, C. Huang, J. Ji, and J. Wu, "Experimental and numerical investigation of the axial behavior of connection in CFST diagrid structures," *Tsinghua Science and Technology*, vol. 13, no. S1, pp. 108–113, 2008.
- [8] S. P. Schneider, "Axially loaded concrete-filled steel tubes," *Journal of Structural Engineering*, vol. 124, no. 10, pp. 1125–1138, 1996.
- [9] H.-T. Hu, C.-S. Huang, M.-H. Wu, and Y.-M. Wu, "Nonlinear analysis of axially loaded concrete-filled tube columns with confinement effect," *Journal of Structural Engineering*, vol. 129, no. 10, pp. 1322–1329, 2003.
- [10] Y. Guo and Y. Zhang, "Comparative study of CFRP-confined CFST stub columns under axial compression," *Advances in Civil Engineering*, vol. 2018, Article ID 7109061, 8 pages, 2018.
- [11] M. H. Lai and J. C. M. Ho, "A theoretical axial stress-strain model for circular concrete-filled-steel-tube columns," *Engineering Structures*, vol. 125, pp. 124–143, 2016.
- [12] F.-X. Ding, L. Fu, and Z.-W. Yu, "Behaviors of axially loaded square concrete-filled steel tube (CFST) stub columns with notch in steel tube," *Thin-Walled Structures*, vol. 115, pp. 196–204, 2017.
- [13] J. Cai, J. Pan, and X. Li, "Behavior of ECC-encased CFST columns under axial compression," *Engineering Structures*, vol. 171, pp. 1–9, 2018.
- [14] X. Lv and W. Lu, "Seismic behavior of concrete-filled rectangular steel tubular columns under cyclic loading," *Journal of Building Structures*, vol. 21, no. 2, pp. 2–11, 2000.
- [15] Y.-G. Zhao, S. Lin, Z.-H. Lu, T. Saito, and L. He, "Loading paths of confined concrete in circular concrete loaded CFT stub columns subjected to axial compression," *Engineering Structures*, vol. 156, pp. 21–31, 2018.
- [16] Z. Liu and S. C. Goel, "Cyclic load behavior of concrete-filled tubular braces," *Journal of Structural Engineering*, vol. 114, no. 7, pp. 1488–1506, 1988.
- [17] C. Hansapinyo, C. Buachart, and P. Chaimahawan, "Tests of inclined concrete-filled steel tubular stub columns under vertical cyclic loading," *Advances in Civil Engineering*, vol. 2018, Article ID 5426731, 9 pages, 2018.



Hindawi

Submit your manuscripts at
www.hindawi.com

